MOX–Report No. 13/2010

A Space-Time Adaptation Scheme for Unsteady Shallow Water Problems

G.M.Porta, Simona Perotto, F. Ballio

MOX, Dipartimento di Matematica "F. Brioschi"
Politecnico di Milano, Via Bonardi 9 - 20133 Milano (Italy)

mox@mate.polimi.it http://mox.polimi.it

A Space-Time Adaptation Scheme for Unsteady Shallow Water Problems

G.M. Porta[♭], S. Perotto[♯], F. Ballio[♭]

April 29, 2010

[♭] D.I.I.A.R., Sezione Idraulica
Politecnico di Milano
Piazza Leonardo da Vinci 32, 20133 Milano, Italy
giovanni.porta@mail.polimi.it
francesco.ballio@polimi.it

[♯] MOX– Modellistica e Calcolo Scientifico
Dipartimento di Matematica "F. Brioschi"
Politecnico di Milano
via Bonardi 9, 20133 Milano, Italy
simona.perotto@polimi.it

Keywords: shallow water equations, mesh adaptation, time step adaptation, recovery based estimator

AMS Subject Classification: 76B15, 65M50, 65M60

Abstract

We provide a space-time adaptation procedure for the approximation of the Shallow Water Equations (SWE). This approach relies on a recovery based estimator for the global discretization error, where space and time contributions are kept separate. In particular we propose an ad hoc procedure for the recovery of the time derivative of the numerical solution and then employ this reconstruction to define the error estimator in time. Concerning the space adaptation, we move from an anisotropic error estimator, i.e., able to automatically identify the density, the shape and the orientation of the elements of the computational mesh. The proposed global error estimator turns out to share the good properties of each recovery based error estimator. The whole adaptive procedure is then combined with a suitable stabilized finite element SW solver. Finally the reliability of the coupled solution-adaptation procedure is successfully assessed on two unsteady test cases of interest for hydraulics applications.

1 Introduction

The main goal pursued by an adaptive computational method is to improve the quality of the numerical discretization of a physical phenomenon via a suitable redistribution of the computational effort on the space-time domain. In general an adaptive method relies on a robust indicator of the computational error, which suggests the criteria driving the adaptation procedure. Both heuristic and theoretically sound indicators are used in practice. Among the heuristic indicators we recall the widely employed recovery based error estimators (see [38, 1]), while the goal oriented error estimators (see, e.g., [2]) excel among the theoretical indicators.

Aim of this paper is to apply a space-time adaptation scheme, driven by a recovery based error estimator, to the numerical discretization of the 2D Shallow Water Equations (SWE). SWE coincide with a system of hyperbolic PDEs, obtained by integrating the Navier Stokes equations over the water depth (see, e.g., [36]). They provide a reference model for physical configurations characterized by large spatial scales in the horizontal plane and considerably smaller scales along the vertical direction: in these cases a two dimensional modeling turns out to be often adequate for a reliable description of the phenomenon at hand. The numerical approximation of the SWE is a recurrent topic in the literature, essentially due to the several relevant applications associated with this model (flood wave propagation, analysis of flux distribution in large rivers, propagation of tidal waves in coastal areas, estuarine dynamics, lake circulation, dam-break modeling etc.). Adaptive techniques are successfully applied to the discretization of SWE in a certain number of works (see, e.g., [26, 17, 29, 15, 6, 19, 27]). Most of these papers focus essentially on the adaptation of the computational mesh only. Isotropic adapted grids are generally employed ([26, 17, 15, 6, 19]), whereas few papers deal with an anisotropic mesh adaptation ([29, 27]). This can be probably ascribed to the more complex setting involved by an anisotropic mesh adaptation, even though the computational advantages yielded by the employment of anisotropic grids are already well established in the literature.

On the contrary a combined space-time adaptation is more rarely used (see, e.g., [26, 17, 15]). Concerning the most recurrent time adaptation strategies, we can distinguish between two approaches: when the solution is approximated via discontinuous methods (for instance, by a discontinuous Galerkin or a finite volume scheme), it is possible to assign elementwise a different time step by resorting to a *local time stepping technique* (see, e.g., [15, 17]); on the other hand, when the discrete solution is continuous in space (e.g., the problem is discretized via a standard Galerkin approximation) a single time step is assigned on the whole mesh (e.g., [26]). In more detail, in [15, 17] the time step is chosen elementwise to guarantee a certain fixed Courant number on each element, even of different size. In [26] a space-time adaptation is applied to the computation of the flow field in the Venice Lagoon. The authors move from a modified Shallow Water system, where the nonlinear advective term is erased from the momentum equa-

tion. This system is then solved through a suitable operator splitting, which induces the time discretization error estimator itself.
The adaptation procedure proposed in this paper relies on an a posteriori estimator for the space-time error, where the space and time contributions are kept distinct. The splitting of these two contributions is a crucial point of the proposed approach and it is in accordance with other works in the literature (see, e.g., [3, 22, 32, 26]). Essentially it allows us to manage separately the space and the time adaptation. In more detail the mesh is adapted on the basis of the recovery based error estimator proposed in [25, 27]: here the standard recovery based framework, originally defined in [38], is suitably modified with the aim of defining an anisotropic error estimator. This yields a computationally cheap problem-independent anisotropic error estimator, successfully validated on different problems, 2D as well as 3D ([7, 8, 25, 27]). We employ the recovery based framework also to propose an a posteriori error estimator for the discretization error in time. Since we discretize the SWE system via a suitable stabilized (continuous) finite element method, a single adapted time step is predicted at each time for the whole set of elements. However we are confident that the proposed approach can be extended in a straightforward way to a local time stepping framework as well as to different problem settings, due to the intrinsic problem-independence of the recovery based error estimators. As far as we know this work represents a first attempt in the literature to combine anisotropic mesh adaptation with time adaptation in the numerical approximation of the SW system.
The paper is organized as follows. In Section 2 we introduce the SWE system and the adopted discretization scheme. Section 3 is devoted to the definition of the space-time recovery based error estimator. The whole space-time adaptive procedure is then detailed in Section 4. The reliability and efficiency of the solution-adaptation coupling is checked in Section 5 on a benchmark test case and real scale hydraulic setting. Concluding remarks are drawn in the last section.

2 The Shallow Water Equations

The SWE system is obtained by integrating the 3D Navier-Stokes equations over the water depth ([36]). This integration is performed after assuming a negligible vertical velocity and acceleration. As a consequence an hydrostatic pressure distribution is understood. SWE are consequently used to model phenomena where the mass and the momentum exchanges are dominant in the planar directions.
In this work we consider the so-called velocity-celerity formulation of the SWE (see, e.g., [27, 30]) given by

$$\frac{\partial \mathbf{U}}{\partial t} + A_1 \frac{\partial \mathbf{U}}{\partial x} + A_2 \frac{\partial \mathbf{U}}{\partial y} = \mathbf{S} \quad \text{in } \Omega, \tag{1}$$

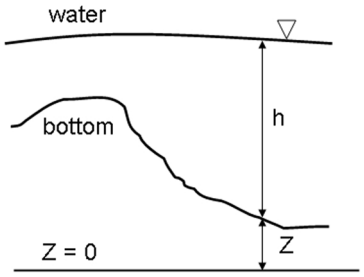

Figure 1: Definition sketch: vertical section.

where Ω is a polygonal domain in $\mathbb{R}^2$. The unknown vector $\mathbf{U} = (u, v, c)^T$ is composed by the x- and y-component of the depth-averaged velocity vector $\mathbf{u} = (u, v)^T$, and by the variable $c = 2\sqrt{gh}$, with g the gravity acceleration and h the total water depth measured with respect to the bottom profile Z (see Figure 1). Quantity c is proportional to the celerity of small perturbations, which, in turn, depends on the water depth. The matrices A_1 and A_2 are defined as

$$A_1 = \begin{bmatrix} u & 0 & \frac{c}{2} \\ 0 & u & 0 \\ \frac{c}{2} & 0 & u \end{bmatrix}, \quad A_2 = \begin{bmatrix} v & 0 & 0 \\ 0 & v & \frac{c}{2} \\ 0 & \frac{c}{2} & v \end{bmatrix},$$

while vector $\mathbf{S}$ includes all the possible sources and sinks of the momentum, which depend on the problem at hand (e.g., friction loss, gravity force, wind stress on free surface, Coriolis force). Typically, in a flood modeling, $\mathbf{S} = \mathbf{S}_0 - \mathbf{S}_f$, where $\mathbf{S}_0 = -\nabla Z$ is the bottom slope (see Figure 1) and $\mathbf{S}_f$ is the friction loss.
From a differential viewpoint, SWE coincide with a system of first order hyperbolic partial differential equations. In particular system (1) is written in a nonconservative form. The three equations constituting the system are dimensionally homogeneous. Moreover matrices A_1 and A_2 are both symmetric: this property makes the velocity-celerity formulation particularly suited to a numerical approximation based on stabilized finite elements, as shown in next section.

2.1 The finite element solver

Following [27], we resort to a streamline-diffusion shock-capturing finite element method (SDSCFEM) to approximate system (1). The streamline-diffusion finite element method was originally proposed in [13] for an advection-diffusion system. In particular this scheme is able to damp the spurious oscillations arising when the standard Galerkin finite element method is employed in an advection-dominated case. A generalization of this method to hyperbolic systems is provided, for instance, in [14, 33]. In a hyperbolic framework it turns out to be crucial to suitably treat also possible shocks and discontinuities of the solution, which may arise even in the presence of smooth boundary and initial data. For

this reason ad hoc shock-capturing terms are usually further added to a stabilized finite element formulation (e.g., [14]).
To provide the SDSCFE approximation of SWE, we move from the weak form of system (1): for any $t \in (0,T]$, find $\mathbf{U} = \mathbf{U}(t) \in [W]^3$, such that

$$\int_\Omega \mathbf{w} \cdot \left(\frac{\partial \mathbf{U}}{\partial t} + A_1 \frac{\partial \mathbf{U}}{\partial x} + A_2 \frac{\partial \mathbf{U}}{\partial y} \right) d\Omega = \int_\Omega \mathbf{w} \cdot \mathbf{S}\, d\Omega \quad \forall \mathbf{w} \in [W]^3, \tag{2}$$

with $\mathbf{w}$ the test function. The functional space W is chosen according to the boundary conditions demanded by the physical configuration at hand. At this level we do not make any specific choice for the boundary conditions, so that we can only state that W is a suitable subspace of the Sobolev space $H^1(\Omega)$ (for the definition of all the functional spaces defined herein see, e.g., [20]).
Let now $\mathcal{T}_h = \{K\}$ be a conformal triangulation of the domain Ω, with h_K the diameter of the generic triangle K, and let $V_{\mathcal{T}_h} = \{V\}$, the set of all the vertices V of $\mathcal{T}_h$ ([4]). Then let $W_h = \left\{ w_h \in C^0(\overline{\Omega}) : w_h|_K \in \mathbb{P}_1(K), \forall K \in \mathcal{T}_h \right\} \cap W$ define the space of the affine finite elements associated with partition $\mathcal{T}_h$, where $\mathbb{P}_1$ is the space of the polynomials of (global) degree less than or equal to one ([28]).
Thus, following [14], the considered semi-discrete formulation of (2) reads: for any $t \in (0,T]$, find $\mathbf{U}_h = \mathbf{U}_h(t) = (u_h, v_h, c_h)^T \in [W_h]^3$, such that

$$\begin{aligned}
&\sum_{K \in \mathcal{T}_h} \int_K \mathbf{w}_h \cdot \left(\frac{\partial \mathbf{U}_h}{\partial t} + A_1 \frac{\partial \mathbf{U}_h}{\partial x} + A_2 \frac{\partial \mathbf{U}_h}{\partial y} \right) dK \\
&+ \sum_{K \in \mathcal{T}_h} \int_K \Theta_K \left(A_1 \frac{\partial \mathbf{w}_h}{\partial x} + A_2 \frac{\partial \mathbf{w}_h}{\partial y} \right) \cdot \left(\frac{\partial \mathbf{U}_h}{\partial t} + A_1 \frac{\partial \mathbf{U}_h}{\partial x} + A_2 \frac{\partial \mathbf{U}_h}{\partial y} \right) dK + \\
&\sum_{K \in \mathcal{T}_h} \int_K \delta_K \frac{\|\mathbf{R}_K\|_2}{\epsilon + \|\nabla \mathbf{U}_h\|_2} \nabla \mathbf{U}_h \cdot \nabla \mathbf{w}_h \, dK = \sum_{K \in \mathcal{T}_h} \int_K \mathbf{w}_h \cdot \mathbf{S}\, dK \\
&+ \sum_{K \in \mathcal{T}_h} \int_K \Theta_K \left(A_1 \frac{\partial \mathbf{w}_h}{\partial x} + A_2 \frac{\partial \mathbf{w}_h}{\partial y} \right) \cdot \mathbf{S}\, dK \quad \forall\, \mathbf{w}_h \in [W_h]^3,
\end{aligned} \tag{3}$$

where $\mathbf{R}_K$ is the elemental residual vector, Θ_K is the stabilization matrix, ϵ and δ_K are suitable tuning parameters of the shock-capturing correction and $\|\cdot\|_2$ denotes the standard Euclidean norm. The second terms on the left- and on the right-hand side of system (3) represent the streamline-diffusion stabilization, weighted by the matrix

$$\Theta_K = \left[\frac{4}{\mu_K^2} \sum_{i=1}^{2} A_i^2 \right]^{-\frac{1}{2}}, \tag{4}$$

where μ_K is a representative dimension of the element K. In the case of uniform meshes the standard choice is $\mu_K = h_K$ ([13]). On the other hand the third term on the right hand side represents the shock capturing correction, expressed as a function of the elemental residual. The tuning parameter δ_K is usually chosen

such that $\delta_K = \mathcal{O}(\mu_K)$, while coefficient ϵ simply prevents a division by zero (it is set to 2.2e-16 in the numerical results in section 5).
Notice that formulation (3) is strongly consistent, since both the streamline-diffusion and the shock-capturing terms vanish when $\mathbf{U}$ replaces $\mathbf{U}_h$.
Finally the semi-discrete formulation (3) is discretized in time through the standard finite difference θ-method (see, e.g., [28]). For this purpose, we introduce a partition of the time window $[0, T]$ by introducing the time levels $\{t^0, \ldots, t^n\}$, which identify the set $\{I_k\}$ of the time intervals I_k of amplitude $\Delta t^k = t^{k+1} - t^k$, for $k = 0, \ldots, n-1$. At the initial time t^0 a suitable initial condition $\mathbf{U}_h^0 \in [W_h]^3$, is imposed. Moreover we choose $\theta = 2/3$ to guarantee the unconditional stability of the θ-scheme, and to prevent the arising of spurious oscillations near the discontinuities of the solution.

3 A recovery based space-time error estimator

The recovery based error estimators were originally proposed in [38] in the framework of linear elasticity. They found on a simple remark: in a finite element modeling, the stresses are usually obtained by differentiating the displacement field; it is consequently a poorer approximation compared with the displacement field itself. To get rid of this limitation, the idea is to improve the accuracy of the numerical gradient by means of suitable re-interpolations and average procedures, known as recovery procedures. These essentially consist of suitable projections of the numerical gradient onto richer spaces. Several recipes have been proposed in the literature for this purpose (see, e.g., [38, 39, 31]). Moreover the L^2-norm of the difference between the recovered and the numerical gradient provides us with a robust a posteriori error estimator for the H^1-seminorm of the discretization error: this estimator can be consequently used to drive a corresponding mesh adaptation procedure (see, e.g., [40]). To summarize two targets are pursued at a time via a recovery based approach: the proposal of a better approximation for the discrete gradient as well as of an a posteriori error estimator for the H^1-seminorm of the error.
Many works in the literature investigate recovery based error estimators, although their theoretical properties are not yet clearly understood (see, e.g., [1, 16, 23, 37]). On the other hand, these estimators have been applied to a wide range of different physical problems, showing a remarkable numerical robustness (see, e.g., [11, 34, 21, 7, 8]). Many good properties are shared by these estimators: for instance, they depend only on the chosen finite element space, being, on the contrary, completely independent of the considered problem, of the governing equations and of the other details characterizing the adopted finite element formulation (e.g., stabilization terms). From a computational point of view they are really cheap and easy to implement, since their definition involves only the numerical solution and its gradient. All these properties make recovery based error estimators very appealing tools with a view to an adaptive procedure.

In particular in this work we resort to this class of estimators to adapt both the space and the time step. We propose an a posteriori recovery based error estimator η^{S-T} to control the global discretization error (i.e., the error due to both the space and time discretization): in more detail, we define

$$\eta^{S-T} = \eta^{S,A} + \eta^{T}, \tag{5}$$

i.e., as the sum of an anisotropic estimator ($\eta^{S,A}$) for the discretization error in space and an estimator (η^{T}) for the discretization error in time. Definition (5) turns out to be ideal with a view to an adaptive procedure able to select, in an automatic way, the time step as well as the computational grid: indeed the key point is to split the space and time contributions, as confirmed by other works in the literature (see. e.g., [35, 3, 22, 32, 24]).
In the sequel we describe separately the space and time contribution to estimator (5). They both understand a recovery based procedure. Notice that, as far as we know, this is the first time that a recovery based error estimator is used for time adaptation in the shallow water framework.

3.1 The anisotropic setting

In this section we provide the minimal background required to found the anisotropic estimator $\eta^{S,A}$. In particular we refer to the anisotropic framework introduced in [9]. To identify the geometric properties of each triangle K in $\mathcal{T}_h$, we move from the geometric transformation of the reference triangle $\widehat{K}$ into the generic triangle K, i.e., from the standard invertible affine map $T_K : \widehat{K} \to K$, given by

$$\mathbf{x} = T_K(\widehat{\mathbf{x}}) = M_K \widehat{\mathbf{x}} + \mathbf{t}_K \quad \forall \mathbf{x} \in K, \tag{6}$$

with $\widehat{\mathbf{x}} \in \widehat{\mathbf{K}}$, and where $M_K \in \mathbb{R}^{2\times 2}$ and $\mathbf{t}_K \in \mathbb{R}^2$. We exploit the spectral properties of the Jacobian M_K, via two successive factorizations: we first introduce the polar decomposition $M_K = B_K Z_K$ of M_K, where $B_K \in \mathbb{R}^{2\times 2}$ is a symmetric positive definite matrix and Z_K is an orthogonal matrix. Then we consider the spectral decomposition $B_K = R_K^T \Lambda_K R_K$ of B_K, where $R_K^T = [\mathbf{r}_{1,K}, \mathbf{r}_{2,K}]$ is the matrix of the right eigenvectors of B_K and $\Lambda_K = \mathrm{diag}(\lambda_{1,K}, \lambda_{2,K})$ is the diagonal matrix of the corresponding eigenvalues. We identify here $\widehat{K}$ with the equilateral triangle inscribed in the unit circle centered at the origin. For this choice the shape and the orientation of each triangle are fully described by the quantities $\mathbf{r}_{i,K}$ and $\lambda_{i,K}$, for $i = 1, 2$. In more detail, the unit circle circumscribing $\widehat{K}$ is mapped into an ellipse circumscribing K (see Figure 2). Then $\mathbf{r}_{1,K}$ and $\mathbf{r}_{2,K}$ identify the principal directions of orientation of the two semi-axes, the major and the minor, respectively while $\lambda_{1,K}$ and $\lambda_{2,K}$ measure the length of these semi-axes.
We introduce the so-called stretching factor $s_K = \lambda_{1,K}/\lambda_{2,K}$ as synthetic indicator of the anisotropy of the triangle K. Without loosing generality, we assume $\lambda_{1,K} \geq \lambda_{2,K}$, so that $s_K \geq 1$ for each K in $\mathcal{T}_h$. In particular $s_K = 1$ in the case of

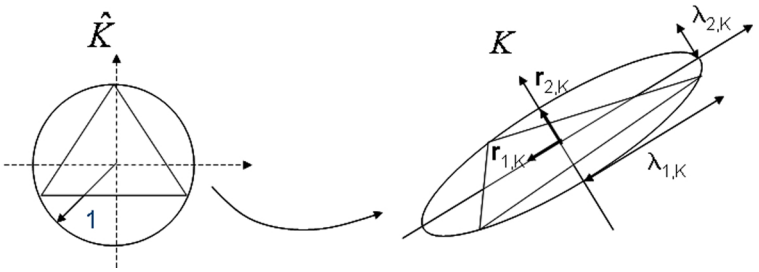

Figure 2: Geometrical interpretation of the map T_K.

an equilateral K. We define also a further geometric scaling factor, which is used to replace parameter μ_K in the stabilization matrix (4). This factor is chosen as the element size along the direction orthogonal to the local flow field. As in an anisotropic mesh the elements may be highly stretched along the directions $\mathbf{r}_{i,K}$, we replace μ_K in the (4) with

$$\lambda_{v,K} = \left[\lambda_{1,K}^{-2} \left(\mathbf{r}_{1,K} \cdot \overline{\mathbf{u}}_K\right)^2 + \lambda_{2,K}^{-2} \left(\mathbf{r}_{2,K} \cdot \overline{\mathbf{u}}_K\right)^2\right]^{-1/2}, \tag{7}$$

where $\overline{\mathbf{u}}_K$ denotes the average of the velocity field $\mathbf{u}$ on the triangle K. The directions $\mathbf{r}_{i,K}$ are thus projected along the local streamline direction, while the weights $\lambda_{i,K}^{-2}$ provide a sort of geometric average.

3.2 The spatial error estimator

To define the a posteriori error estimator $\eta^{S,A}$ for the discretization error in space, we resort to the anisotropic estimator, proposed in [25]. To introduce it, we refer to a general scalar variable z and to its finite element approximation z_h: in our specific case z will coincide with a component of the unknown vector $\mathbf{U}(t) = (u, v, c)^T$ or with a suitable scalar quantity related to its components (e.g., the water depth).
Our goal is to provide, for each time $t > 0$, a fully computable estimation for the H^1-seminorm of the discretization error $e_h^z(t) = z(t) - z_h(t)$, given by

$$|e_h^z(t)|^2_{H^1(\Omega)} = \int_\Omega |\nabla z(t) - \nabla z_h(t)|^2 \, d\Omega. \tag{8}$$

In the spirit of a recovery based approach, we aim at replacing the unknown gradient ∇z with a corresponding recovered gradient and using the right hand side of (8) as the desired error estimator. In particular we look for an anisotropic error estimator, that is defined in terms of the geometric properties of the triangles K. To balance the additional computational effort demanded by an anisotropic analysis, we move from a recovery procedure really simple, different with respect to the standard ones (see, e.g., the procedures proposed in [38, 39, 31]). Let us consider the triangle K and the associated patch Δ_K of elements sharing with

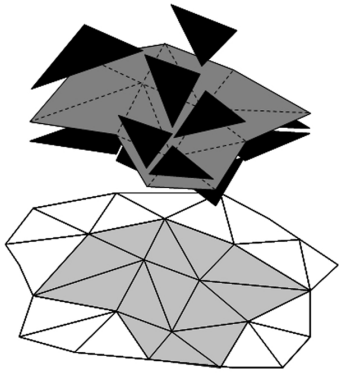

Figure 3: Gradient of the discrete solution (black) and recovered gradient (9) (grey).

K at least a vertex. The recovered gradient $P_R(z_h)(t)$ is thus defined, for each $t > 0$, as

$$P_R(z_h)(\mathbf{x}, t) = \frac{\sum_{K \in \Delta_K} \nabla z_h(t)|_K \cdot |K|}{|\Delta_K|} \quad \forall \mathbf{x} \in K, \tag{9}$$

i.e., it coincides with the area-weighted average of the gradient of the solution, computed on the triangles belonging to the patch Δ_K. With a view to the whole solving-adaptive procedure, time t will coincide with the discrete times t^k of the partition $\{I_k\}$. Formula (9) yields a piecewise constant recovered gradient, i.e., a quantity which is in general poorer compared with the standard piecewise linear recovered gradients in [38, 39, 31]. However, notice that, as discussed in [25], procedure (9) can be enhanced to higher polynomial degree. Here we adopt the simplest choice.

The local estimator is then defined, for each $t > 0$, as the L^2-norm on the patch Δ_K of the discard between the gradient of the numerical solution and the recovered gradient, extended to the whole patch Δ_K (see Figure 3), i.e., as

$$\left[\eta_K^I(t)\right]^2 = \int_{\Delta_K} |P_R(z_h)_{K \to \Delta_K}(t) - \nabla z_h(t)|^2 \, d\Delta_K, \quad \forall K \in \mathcal{T}_h. \tag{10}$$

At this level no geometric quantity related to the element K appears in the estimator (10) as well as in the recovery procedure (9). The superscript I stands for isotropic indeed. Moreover notation $P_R(z_h)_{K \to \Delta_K}$ refers to the extension of value (9) from K to the whole patch Δ_K. Notice that in (10) both $P_R(z_h)(t)$ and $\nabla z_h(t)$ are constant, global and piecewise, respectively. In this respect we state that the proposed recovery procedure is poorer than the standard ones ([38, 39, 31]). On the other hand it is simpler to implement and the source of information involved in (9) is wider: estimator η_K^I is indeed computed on set of elements larger compared with the patch usually employed, i.e., the patch

associated with a vertex of $\mathcal{T}_h$. Estimator (10) quantifies the variance of the gradient on Δ_K, with respect to the area-weighted average. The corresponding global error estimator thus coincides with

$$\left[\eta^I(t)\right]^2 = \sum_{K\in\mathcal{T}_h} \left[\eta^I_K(t)\right]^2 \quad \forall t > 0. \tag{11}$$

We follow now [25] to derive an anisotropic counterpart of estimator $\eta^I_K(t)$. Moving from the anisotropic framework introduced in section 3.1, the local anisotropic estimator can be defined, for any $K \in \mathcal{T}_h$ and for any $t > 0$, as

$$\left[\eta^A_K(t)\right]^2 = \frac{1}{\lambda_{1,K}\lambda_{2,K}} \int_{\Delta_K} \Big\{ \lambda^2_{1,K} \left[\mathbf{r}_{1,K} \cdot (P_R(z_h)_{K\to\Delta_K}(t) - \nabla z_h(t))\right]^2 + \\ + \lambda^2_{2,K} \left[\mathbf{r}_{2,K} \cdot (P_R(z_h)_{K\to\Delta_K}(t) - \nabla z_h(t))\right]^2 \Big\} d\Delta_K. \tag{12}$$

The idea is essentially to project the isotropic estimator (10) onto the anisotropic directions $\mathbf{r}_{1,K}$ and $\mathbf{r}_{2,K}$. Notice that estimators η^I_K and η^A_K are equivalent when $\lambda_{1,K} = \lambda_{2,K}$. The scaling factor $(\lambda_{1,K}\lambda_{2,K})^{-1}$ is introduced to make estimator η^A_K independent of the element size. The anisotropic global error estimator is then given by

$$\left[\eta^A(t)\right]^2 = \sum_{K\in\mathcal{T}_h} \left[\eta^A_K(t)\right]^2 \quad \forall t > 0. \tag{13}$$

Estimator (13) is essentially heuristic. As showed in [25], the idea behind η^A is to mimic, in a recovery based spirit, the anisotropic interpolation error estimate derived in [9] for a Clément-like interpolant of degree one ([5]). Some further rationale behind estimator (13) can be found in [25]. Robustness of estimator η^A is numerically investigated on two dimensional elliptic problems in [25, 27] as well as on the SWE system in [27]. Moreover an extension of η^A to the three-dimensional framework is provided and numerically assessed in [7, 8].

3.3 The time error estimator

We propose a recovery based error estimator also to control the discretization error in time. The idea is similar to the one followed in the previous section, even though we now deal with a 1D setting. In particular the goal pursued is to predict, at each time level, the time step to be used in the next time advancement. This remark immediately relieves us from defining necessarily a global estimator of the time discretization error.

As in previous section we refer to a generic scalar variable z and to its corresponding discretization z_h: at the generic time level t^k, we know z_h at each time level t^j, with $j \in \{0, \dots, k\}$. Then, for each $\mathbf{x} \in \Omega$, we look for an estimator of the discretization error

$$|e^z_h(\mathbf{x})|^2_{H^1(\Delta t^{k-1})} = \int_{I_{k-1}} \left| \frac{\partial z(\mathbf{x})}{\partial t} - \frac{\partial z_h(\mathbf{x})}{\partial t} \right|^2 dt, \tag{14}$$

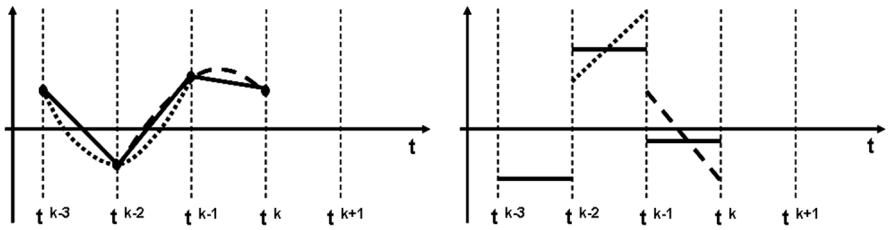

Figure 4: Time derivative recovery procedure: recovered solution z^* (dotted and dashed lines) versus linear interpolant of values z_h^j (continuous line) on the left; comparison between the time derivatives $\partial z^*/\partial t$ (dotted and dashed lines) and $\partial z_h/\partial t$ (continuous lines) on the right.

to predict the next time step Δt^k, with $e_h^z = z - z_h$, defined as in (8). Notice that this seminorm is not dimensionless as the H^1-seminorm in (8).
To compute the derivative $\partial z_h(\mathbf{x})/\partial t$ in (14), we move form the pointwise values $z_h^j = z_h(\mathbf{x}, t^j)$, with $j \in \{0, \ldots, k\}$. In particular we replace function z_h on the interval I_{k-1}, for $k = 1, \ldots, n$, with the straight line interpolating at t_{k-1} and t_k the values z_h^{k-1}) and z_h^k, respectively. We compute

$$\left.\frac{\partial z_h(\mathbf{x})}{\partial t}\right|_{I_{k-1}} = \frac{z_h^k - z_h^{k-1}}{\Delta t^{k-1}}.$$

Then the idea is to substitute the time derivative $\partial z/\partial t$ of the exact solution on I_{k-1} with the time derivative $\partial z^*/\partial t$ of a suitable recovered solution z^*. In particular we build the parabola z^* interpolating the couples of values (t^{k-2}, z_h^{k-2}),(t^{k-1}, z_h^{k-1}),(t^k, z_h^k) (see Figure 4, left) and then we assume

$$\left.\frac{\partial z(\mathbf{x})}{\partial t}\right|_{I_{k-1}} \equiv \left.\frac{\partial z^*(\mathbf{x})}{\partial t}\right|_{I_{k-1}} \quad \forall\, k = 1 \ldots n. \tag{15}$$

In this way we obtain a piecewise linear recovered time derivative (see Figure 4, right). According to a standard recovery based approach, the recovered derivative is now a polynomial of higher degree with respect to the discrete derivative $\partial z_h/\partial t$.
The local recovery based time estimator is thus defined as

$$\left[\eta^T_{I_{k-1}}(\mathbf{x})\right]^2 = \widetilde{T} \int_{I_{k-1}} \left| \left.\frac{\partial z^*(\mathbf{x})}{\partial t}\right|_{I_{k-1}} - \frac{z_h^k - z_h^{k-1}}{\Delta t^{k-1}} \right|^2 dt, \tag{16}$$

where $\widetilde{T}$ is a suitable time scale factor characteristic of the problem at hand. Factor $\widetilde{T}$ essentially makes estimator $\eta^T_{I_{k-1}}(\mathbf{x})$ dimensionless, i.e., suited to be added to the space estimator $\eta^{S,A}$, according to the space-time splitting in (5). A possible choice for $\widetilde{T}$ is the ratio $L/\tilde{c}$ where L is a characteristic length of the domain and $\tilde{c}$ is a representative value for the celerity. As an alternative $\widetilde{T}$ could

coincide with the time step Δt^{k-1} itself.
From a computational viewpoint estimator (16) is computed on each vertex V of the current grid $\mathcal{T}_h$. Of course we aim at providing a unique estimate of the time discretization error at time t^k, by merging all the spatially distributed information in a single indicator. For this reason, we first compute an average value of the estimator on each triangle K as

$$\left[\eta^T_{I_{k-1},K}\right]^2 = \frac{\sum_{V\in K}\left[\eta^T_{I_{k-1}}(V)\right]^2}{3}.$$

Then the time error estimator associated with the interval I_{k-1} is computed as

$$\eta^T_{I_{k-1}} = \sqrt{\sum_{K\in\mathcal{T}_h^k}\left[\eta^T_{I_{k-1},K}\right]^2}. \tag{17}$$

As explained in section 4.2, estimator (17) will be used in a predictive fashion to identify the successive time step Δt^k.

4 The solving-adaptive procedure

In this section we detail the proposed space-time adaptive procedure, which combines the information provided by the spatial and temporal a posteriori error estimators in (13) and (17) to drive an automatic choice of the spatial and temporal steps. For this purpose we refer to (5) and we introduce the global error estimator η^{S-T}, with $\eta^{S,A} \equiv \eta^A$, and

$$\eta^T = \sum_{k=1}^{n} \eta^T_{I_{k-1}} \tag{18}$$

the global a posteriori error estimator in time induced by (17). Since the θ-scheme employed for the time discretization assumes a progressive time advancement, estimator η^T becomes meaningful only at the end of the numerical simulation, i.e., when the discrete solution is known at each time level. This is the reason why, during the adaptive procedure, we resort to the local counterpart (17).
Our purpose is now to control η^{S-T} by assigning a global tolerance τ which we split as $\tau = \tau^S + \tau^T$, where τ^S and τ^T are the tolerances demanded on $\eta^{S,A}$ and η^T, respectively. The two adaptation procedures are described separately. The algorithm merging the two adaptive schemes with the discrete solver is tackled in section 4.3.

4.1 The mesh adaptation scheme

We use here the mesh adaptation procedure proposed in [10] and then successfully employed in several works (see, e.g., [23, 24, 27]).

The crucial point is to derive a so-called metric identifying the new adapted mesh moving from the proposed estimator η^A. In particular we aim at minimizing the number of mesh elements while guaranteeing a prescribed tolerance on η^A, i.e., on the spatial discretization error.
We recall that a metric is represented by a symmetric positive definite tensor field $\widetilde{M} : \Omega \to \mathbb{R}^{2\times 2}$. This tensor can be diagonalized as $\widetilde{M} = \widetilde{R}^T \widetilde{\Lambda}^{-2} \widetilde{R}$, with $\widetilde{\Lambda} = \mathrm{diag}(\widetilde{\lambda_1}, \widetilde{\lambda_2})$ a positive diagonal matrix, and $\widetilde{R}^T = [\widetilde{\mathbf{r}}_1, \widetilde{\mathbf{r}}_2]$ an orthonormal tensor. Given a background triangulation $\mathcal{T}_h$, we can always approximate the pointwise matrices $\widetilde{\Lambda}$ and $\widetilde{R}$ with suitable piecewise constant quantities on $\mathcal{T}_h$, i.e., such that $\widetilde{\lambda}_i|_K = \widetilde{\lambda}_{i,K}$, $\widetilde{\mathbf{r}}_i|_K = \widetilde{\mathbf{r}}_{i,K}$, for any $K \in \mathcal{T}_h$ and with $i = 1, 2$.
Now our first step consists of deriving a piecewise constant optimal metric on a background mesh, by exploiting the information provided by estimator η^A evaluated on $\mathcal{T}_h$ itself. For this purpose we suitably rewrite the local estimator (12). To simplify the notation we omit hereafter the dependence on time. We introduce the so called *recovered gradient matrix* given by,

$$[G_{\Delta_K}]_{i,j} = \int_{\Delta_K} \{P_R(z_h)_{K\to\Delta_K} - \nabla z_h\}_i \{P_R(z_h)_{K\to\Delta_K} - \nabla z_h\}_j \, d\Delta_K \qquad (19)$$

for $i, j = 1, 2$. Moreover, we define a scaled recovered gradient matrix $\widehat{G}_{\Delta_K} = G_{\Delta_K}/|\Delta_K|$, with $|\Delta_K| = \lambda_{1,K}\lambda_{2,K}|\widehat{\Delta}_K|$ and where $\widehat{\Delta}_K = T_K^{-1}(\Delta_K)$ is the pull-back of the patch Δ_K via map T_K. Estimator η_K^A can thus be written as

$$[\eta_K^A]^2 = |\widehat{\Delta}_K|\lambda_{1,K}\lambda_{2,K} \left\{ s_K \left(\mathbf{r}_{1,K}^T \widehat{G}_{\Delta_K} \mathbf{r}_{1,K} \right) + s_K^{-1} \left(\mathbf{r}_{2,K}^T \widehat{G}_{\Delta_K} \mathbf{r}_{2,K} \right) \right\}. \qquad (20)$$

Notice that in this last expression the information concerning the size of the element K is essentially lumped into the multiplicative constant $|\widehat{\Delta}_K|\lambda_{1,K}\lambda_{2,K}$, at least asymptotically (i.e., when the mesh is sufficiently fine). Thus maximize the area of K (which is equivalent to minimize the number of elements of $\mathcal{T}_h$) leads to minimize the term in brackets. We solve consequently the following local constrained minimization problem: find $(s_K, \mathbf{r}_{1,K})$ such that

$$I(s_K, \mathbf{r}_{1,K}) = s_K \left(\mathbf{r}_{1,K}^T \widehat{G}_{\Delta_K} \mathbf{r}_{1,K} \right) + s_K^{-1} \left(\mathbf{r}_{2,K}^T \widehat{G}_{\Delta_K} \mathbf{r}_{2,K} \right) \quad \text{is minimum,} \quad (21)$$

with $s_K \geq 1$, $\|\mathbf{r}_{1,K}\|_2 = \|\mathbf{r}_{2,K}\|_2 = 1$, $\mathbf{r}_{1,K} \cdot \mathbf{r}_{2,K} = 0$. In [23] a proof of the existence and the uniqueness of the solution to problem (21) is provided. In particular the optimal stretching factor $\widetilde{s}_K$ and direction $\widetilde{\mathbf{r}}_{1,K}$ are given by $\widetilde{s}_K = [\sigma_{1,K}/\sigma_{2,K}]^{1/2}$ and $\widetilde{\mathbf{r}}_{1,K} \equiv \mathbf{p}_{2,K}$, where $\sigma_{1,K}$ and $\sigma_{2,K}$ are the eigenvalues of $\widehat{G}_{\Delta_K}$, with $\sigma_{1,K} \geq \sigma_{2,K}$ and $\mathbf{p}_{2,K}$ is the eigenvector associated with $\sigma_{2,K}$. To fully identify the optimal metric, we still need to compute the two optimal values $\widetilde{\lambda}_{1,K}$ and $\widetilde{\lambda}_{2,K}$, separately. These are obtained through an error equidistribution principle: given the global tolerance τ^S, we impose that $\eta_K^A = \tau_K = \tau^S/N_{el}$, for any $K \in \mathcal{T}_h$, where N_{el} is the cardinality of mesh $\mathcal{T}_h$. This yields $\widetilde{\lambda}_{1,K} = \sqrt{\widetilde{s}_K q}$,

$\widetilde{\lambda}_{2,K} = \sqrt{q/\widetilde{s}_K}$, with

$$q = \widetilde{\lambda}_{1,K}\widetilde{\lambda}_{2,K} = \frac{\tau_K^2}{|\widehat{\Delta}_K|\left(\widetilde{s}_K\sigma_{2,K} + \widetilde{s}_K^{-1}\sigma_{1,K}\right)}. \tag{22}$$

Next step is to build the new adapted mesh moving from the just computed optimal metric and the background grid $\mathcal{T}_h$. This goal is achieved via the so called *matching criterion* introduced, for instance, in [23].
Two corrections are imposed during the metric generation process. A minimum value is imposed on the quantity q, to avoid an excessive clustering of mesh elements in correspondence with the solution discontinuities. In more detail, the value q is computed first via (22); then we set $q = \max(q_{min}, q)$, where q_{min} coincides, for instance, with the mean area of the elements of a reference grid.
A second troublesome occurrence which calls for a suitable metric correction is the generation of too coarse meshes. In this case we implement an automatic metric correction procedure. Starting from the optimal metric $\widetilde{M}$ identified by the quantities $\widetilde{\lambda}_{i,K}$, $\widetilde{\mathbf{r}}_{i,K}$ defined above, we predict the number of elements of the adapted mesh $\mathcal{T}_h^{NEW}$ matching $\widetilde{M}$; if this number is less than a chosen threshold $N_{el,min}$, then a new metric $\widetilde{M}^{(1)}$ is proposed on the basis of $\widetilde{M}$ itself. Essentially metric $\widetilde{M}^{(1)}$ is obtained by means of a global and uniform scaling of the tensor $\widetilde{M}$.
The constraints on the minimal element area and number of elements lead to control, from below and from above, the lengths $\lambda_{i,K}$. Anyway both these bounds are such that the local anisotropy, predicted by the optimal metric $\widetilde{M}$ for the mesh elements, is preserved.
To summarize the mesh adaptation is performed through the following iterative procedure. At each iteration k, i.e., at each time level t^k, we solve the differential problem at hand on the mesh $\mathcal{T}_h^k$ and evaluate the a posteriori error estimator η^A on this mesh. Then the optimal metric $\widetilde{M}^{k+1}$ is computed by solving the local constrained optimization problems (21) and via the error equidistribution criterion. We apply the two controls on the area and on the predicted number of mesh elements. Finally the new adapted mesh $\mathcal{T}_h^{k+1}$ matching $\widetilde{M}^{k+1}$ is generated via the matching criterion, i.e., in practice by resorting to the two dimensional metric-based mesh generator BAMG ([12]). In particular at each adaptation step a complete remesh is performed, even though BAMG, as far as possible, preserves the previous position of mesh nodes during the adaptation procedure.

4.2 The time adaptation scheme

The time adaptation procedure is driven through the imposition of a local tolerance instead of the global tolerance τ^T. Indeed the global error estimator (18) cannot be directly used, since it is computable only at the final time $t^n = T$. The time step is thus adapted independently for any time interval, i.e., at each time t^k we aim at predicting the time step Δt^k which identifies the new time

t^{k+1}. This means that the partition of the time window $[0,T]$ as well as the computational mesh at each t^k are among the unknowns of the problem at hand.
We fix consequently a tolerance $\tau^T_{\Delta t}$ for the time local discretization error in time, i.e., (17). We rewrite $\eta^T_{I_{k-1}}$ as

$$\left[\eta^T_{I_{k-1}}\right]^2 = \sum_{K\in\mathcal{T}_h^k}\left[\eta^T_{I_{k-1},K}\right]^2 = \widetilde{T}\left[\Delta t^{k-1}\widetilde{\rho}^T_{I_{k-1}}\right]^2, \tag{23}$$

where

$$\left[\widetilde{\rho}^T_{I_{k-1}}\right]^2 = \frac{1}{[\Delta t^{k-1}]^2}\sum_{K\in\mathcal{T}_h^k}\frac{1}{3}\sum_{V\in K}\left\{\int_{I_{k-1}}\left|\left.\frac{\partial z^*(V)}{\partial t}\right|_{I_{k-1}} - \frac{z_h^k - z_h^{k-1}}{\Delta t^{k-1}}\right|^2 dt\right\}.$$

Since the computational grid changes at each time step, we denote with $\mathcal{T}_h^k$ the mesh corresponding to time level t^k following the notation of the previous section.
We use now the estimator $\eta^T_{I_{k-1}}$ in (23) to predict the new time step Δt^k. We impose $\eta^T_{I_{k-1}} = \tau^T_{\Delta t}$ to we get as new time step the value

$$\Delta t^k = \sqrt{\frac{1}{\widetilde{T}}}\frac{\tau^T_{\Delta t}}{\widetilde{\rho}^T_{I_{k-1}}}. \tag{24}$$

Value (24) is finally compared with two limit values, Δt_{min} and Δt_{max}, chosen a priori as functions of the time scales characterizing the problem at hand, with the aim of improving the stability and the reliability of the adaptive simulation process. Since estimator $\eta^T_{I_{k-1}}$ can be computed only when the solution is known at three times t^k, t^{k-1}, t^{k-2}, we adapt the time step according to (24) only for $t^k \geq t^2$. As a consequence the size of the first two time steps has to be assigned a priori: in particular we set here $\Delta t^0 = \Delta t^1 = \Delta t_{min}$.

4.3 The solution-adaptation coupling

We provide in Figure 5 a sketch of the algorithm used to combine the discrete solver in section 2.1 with the space and time adaptation steps detailed in section 4.1 and 4.2, respectively.
The simulation starts from an initial condition $\mathbf{U}_h^0$ defined on a sufficiently fine background grid $\mathcal{T}_h^0$. Let us first assume to be at time t^{k-1}, i.e., to know the approximate solution $\mathbf{U}_h^{k-1}$, the mesh $\mathcal{T}_h^{k-1}$ and the time step Δt^{k-1} predicted at the previous iteration. As first concern, we have to suitably linearize the variational formulation (3). For this purpose we solve problem (3) on the grid $\mathcal{T}_h^{k-1}$, with a time step equal to Δt^{k-1} and using $\mathbf{U}_h^{k-1}$ for the linearization. This first step yields a first approximate solution $\mathbf{U}_h^{*k}$ at $t = t^k$. One component of $\mathbf{U}_h^{*k}$ (or a suitable function of its components) can now be used to build estimator

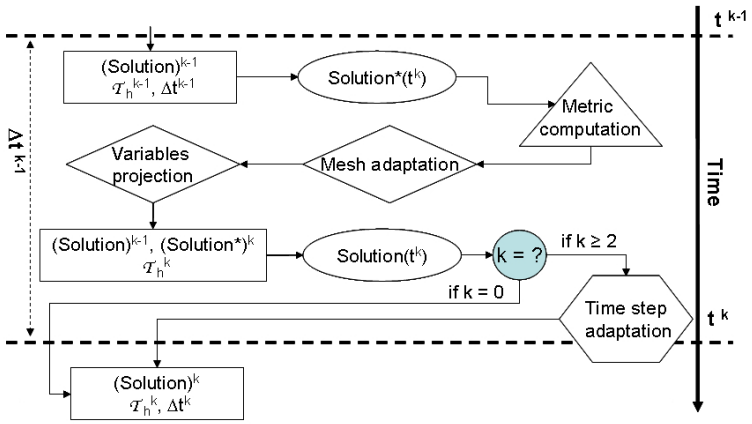

Figure 5: Sketch of the solution-adaptation algorithm.

η^A in (13) for $t = t^k$ and consequently to compute the new metric $\widetilde{M}^k$, via the procedure detailed in section 4.1. This metric is then furnished to BAMG to build the new adapted mesh $\mathcal{T}_h^k$, matching $\widetilde{M}^k$. Now, before proceeding, all the variables evaluated on $\mathcal{T}_h^{k-1}$ have to be projected on the new mesh $\mathcal{T}_h^k$. This operation is accomplished exactly as in [27], i.e., by solving the following problem

$$\sum_{K \in \mathcal{T}_h^k} \int_K (z_h^k - z_h^{k-1}) \cdot w_h^k dK = 0, \tag{25}$$

where z_h^i stands for the generic discrete variable z_h of $\mathbf{U}_h$ evaluated at time t^i, with $i = k-1, k$, while w_h^k denotes the generic finite element test function associated with the adapted mesh $\mathcal{T}_h^k$. Problem (25) is implemented via a dedicated algorithm in FreeFEM++. As numerically shown in [27], procedure (25) ensures the conservation of the mass and the momentum up to a satisfying tolerance.
The SW system is then solved for the second time but now on the mesh $\mathcal{T}_h^k$, and by using this time $\mathbf{U}_h^{*k}$ for the linearization. This second resolution step yields the final vector of unknowns $\mathbf{U}_h^k$ at $t = t^k$. At this point the new time step Δt^k is predicted via recipe (24) and the successive time slab (t^k, t^{k+1}) is thus identified.

5 Numerical results

5.1 Radial dam-break

We consider a radial dam break problem. This test case is a standard benchmark in the SWE literature (see, e.g., [18, 29]). The initial condition is represented by a circular dam, placed in the center of a squared domain and surrounded by

wall boundaries. In our case the domain Ω coincides with a square of side 5m, centered at the origin. We set, at $t = 0$s,

$$\begin{cases} h = 2\text{m} & \text{for } r \leq 0.5\text{m} \\ h = 1\text{m} & \text{for } r > 0.5\text{m}, \end{cases} \tag{26}$$

with $r = \sqrt{(x^2 + y^2)}$, and $u = v = 0$ in the whole domain. The bottom is flat and smooth, so that no source term is considered. Boundary conditions impose $\mathbf{u} \cdot \mathbf{n} = 0$ on the whole boundary. We consider $g = 1$, following [18, 29]. Such a choice affects the celerity of the waves, but does not modify the main features of the whole process. We consider the time window $t \in [0, 1.5]$s.
In Figure 6 we show for three different times the water depth h computed on the grids yielded by adaptive procedure detailed in section 4.3. We make the following choices for the parameters tuning the mesh adaptation: $\tau^S = 1$m, $q_{min} = 2 \times 10^{-4}\text{m}^2$, $N_{el,min} = 1000$. Concerning the time step adaptation we set $\Delta t^0 = 0.003$s and $\Delta t_{max} = 0.04$s. We show only the top-right quarter of the domain, due to the radial symmetry of the problem. In the first part of the phenomenon the solution is characterized by a shock-wave traveling outwards, and by a rarefaction wave traveling inwards. The dynamics of this first phase is very similar to that characterizing a one dimensional dam-break; however, in the radial case, the water depth is variable in the region comprised between the rarefaction and the shock position. This is due to the fact that the fluid is spreading out. Once the rarefaction wave reaches the origin, all the water has been accelerated outwards and the water depth consequently falls below the value $h = 1$m (see Figure 6, left). This induces negative velocities along the radius, for $t > 0.75$s. The radial symmetry of the problem imposes $U = 0$ at $r = 0$, so that the fluid moving inwards is suddenly stopped at the origin. For $t > 1$s this gives rise to a second shock-wave traveling outwards (see Figure 6, center), while the first shock-wave travels undisturbed outwards for the whole considered time window. The two shock waves reduce their amplitude as they propagate, due to the radial spreading of the mass and of the momentum (see Figure 6, right).

In the following we analyze in more detail the performance of the solution-adaptation procedure proposed in section 4.3. We perform first a sensitivity analysis with respect to the value chosen for the local tolerance $\tau^T_{\Delta t}$. In particular Figure 7 shows the time evolution of the time step (left) and of the cardinality of the adapted meshes (right) associated with the choices $\tau^T_{\Delta t} = 0.25$m and $\tau^T_{\Delta t} = 0.5$m, all the remaining parameters being fixed to the values listed above. The trend of the time step is clearly different: as expected, a smaller tolerance induces reduced time steps. For $\tau^T_{\Delta t} = 0.25$m the time step remains about constant around $\Delta t = 0.005$s for $t < 1$s; then it grows, up to $\Delta t = 0.012$s. On the other hand, for $\tau^T_{\Delta t} = 0.5$m, the time step grows continuously, up to the maximal allowed value $\Delta t^{max} = 0.04$s, reached at about $t \approx 1.1$s. In both the cases the time step grows as time advances, even though the variation rate

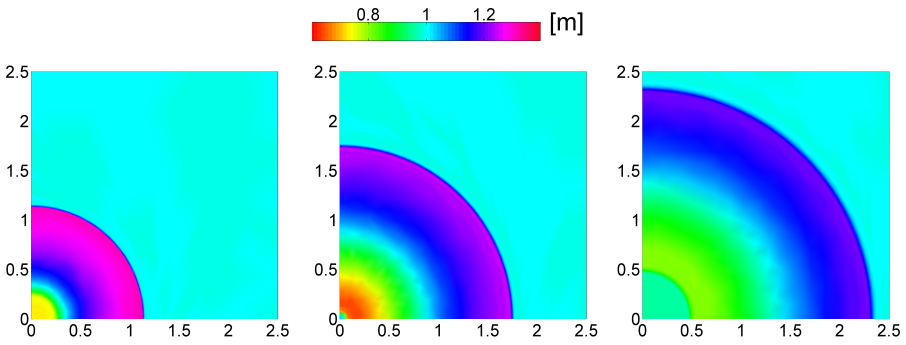

Figure 6: Radial Dam Break: snapshots of the numerical solution at $t = 0.5$s (left), $t = 1$s (center), $t = 1.5$s (right).

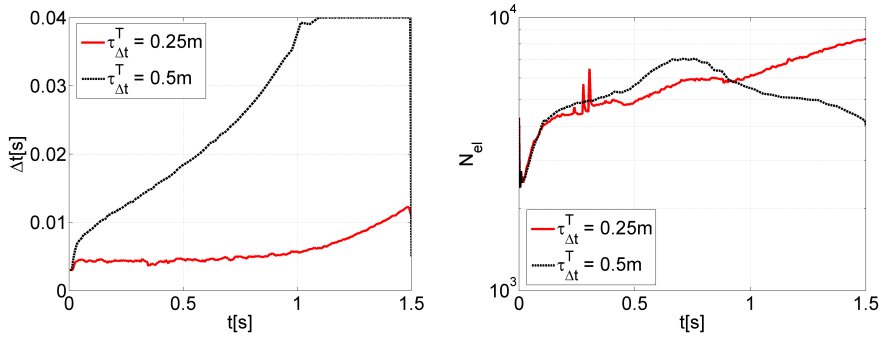

Figure 7: Radial dam break: temporal evolution of the adapted time step (left) and of the cardinality of the adapted grid (right) for two different choices of $\tau^T_{\Delta t}$.

is definitely higher for $\tau^T_{\Delta t} = 0.5$m. This progressive increase is coherent with the evolution of the phenomenon features. During the considered time window, the flow is dominated by the presence of the shock waves, but their amplitude decreases with time, due to the spreading of the fluid. As a consequence, the value of the time error estimator decreases across the discontinuities.
Since the spatial tolerance τ^S is the same for the two simulations, the cardinality of the meshes is of the same order of magnitude in the two cases, i.e., N_{el} varies between a minimum value equal to 3000 and a maximum value equal about to 8000. However, notice that the two trends in Figure 7, right, are different: for $t \leq 0.9$s, a larger number of elements is associated with $\tau^T_{\Delta t} = 0.5$m, while the situation is exactly reversed for $t > 0.9$s. Moreover, the number of elements continuously grows for $\tau^T_{\Delta t} = 0.25$m, while it exhibits a drastic reduction (approximately the 40% for $t \in (0.75, 1.5)$s) for $\tau^T_{\Delta t} = 0.5$m. This is due to the interplay between space and time adaptation and, in part, to the recovery based procedure used to build the estimator.

To clarify this issue we compare the two adapted solutions with a reference

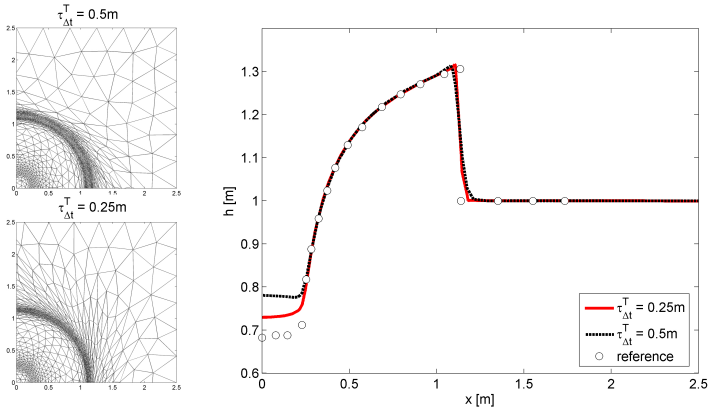

Figure 8: Radial dam break, $t = 0.5$s: adapted computational mesh for $\tau^T_{\Delta t} = 0.5$m (top-left) and $\tau^T_{\Delta t} = 0.25$m (bottom-left) and comparison of the adapted solutions with the reference solution (right).

solution, along a radial section. In particular we adopt as reference solution the one in [18], obtained by solving the problem at hand via a 1D radial SWE system, discretized by a finite volume scheme. Figures 8-10 (right) show the results of such a comparison in terms of water depth for the three times $t = 0.5$s, $t = 1$s and $t = 1.5$s. Moreover we show the adapted meshes associated with the two choices $\tau^T_{\Delta t} = 0.5$m (top-left) and $\tau^T_{\Delta t} = 0.25$m (bottom-left).

Figure 8 refers to time $t = 0.5$s. The two adapted meshes are rather similar (see Figure 8, left): a first refinement appears in correspondence with the front of the shock-wave propagating outwards ($r \approx 1.1$m), while a second less evident refined area is identified at $r \approx 0.2$m. This latter refinement tracks the drop of the water depth due to the rarefaction wave propagation. In this same area both the adapted solutions exhibit a phase difference with respect to the reference solution (see Figure 8, right). Such difference is about 0.05m for $\tau^T_{\Delta t} = 0.25$m and 0.1m for $\tau^T_{\Delta t} = 0.5$m. Since the two adapted meshes are very similar in this zone, we ascribe the phase-difference to the chosen time step only. The shock wave is identified at the same position by both the adaptive simulations. For $\tau^T_{\Delta t} = 0.5$m a slight overdiffusion is present, while the shock wave front is sharply detected for the choice $\tau^T_{\Delta t} = 0.25$m. This remark justifies the difference in terms of mesh cardinality between the two adapted solutions (see Figure 7, right).

Time $t = 1$s is considered in Figure 9. For both the adapted meshes the refined area near the origin reduces to a very small circle. Indeed, at this time, the second shock wave is just starting from this location. In this area the dynamics is not very well captured by both the adaptive solutions; however when the tolerance $\tau^T_{\Delta t}$ reduces, the accuracy of the approximate solution remarkably improves. As for $t = 0.5$s, the position of the shock wave front coincides in the two cases; however the solution associated with $\tau^T_{\Delta t} = 0.5$m exhibits an overdif-

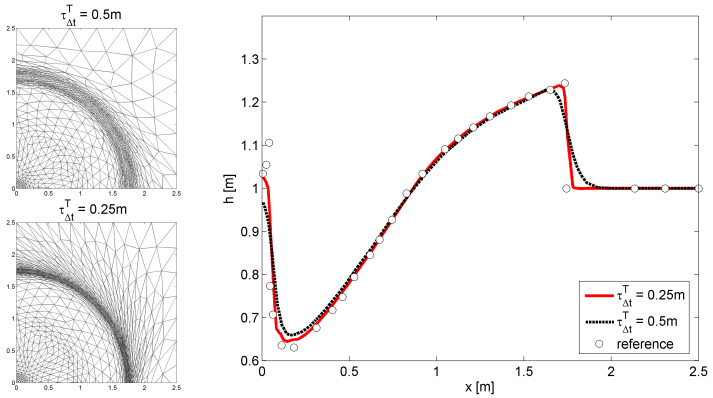

Figure 9: Radial dam break, $t = 1$s: adapted computational mesh for $\tau^T_{\Delta t} = 0.5$m (top-left) and $\tau^T_{\Delta t} = 0.25$m (bottom-left) and comparison of the adapted solutions with the reference solution (right)..

fusion, more evident with respect to the one in Figure 8. On the contrary the steep front is well captured for $\tau^T_{\Delta t} = 0.25$m. This different behaviour finds a counterpart in the thickness of the mesh refinement detected around $r \approx 1.7$m. The global number of elements of the two meshes is really similar for this time (see Figure 7, right). However, it is evident from Figure 9, left, that a lot of elements are clustered in the thin refined area for the choice $\tau^T_{\Delta t} = 0.25$m, while they are more spread for $\tau^T_{\Delta t} = 0.5$m.

At $t = 1.5$s (Figure 10) the difference between the two adapted solutions is more striking: a strong overdiffusion characterizes the shock waves front associated with the choice $\tau^T_{\Delta t} = 0.5$m. On the contrary steep fronts are detected by the choice $\tau^T_{\Delta t} = 0.25$m. Indeed although the spatial tolerance τ^S is the same, the number of elements of the adapted mesh halves by doubling $\tau^T_{\Delta t}$.

This behaviour is linked to the interplay existing between the recovery based space and time adaptation. In particular the overdiffusion seems to be directly proportional to the space and to the time discretization step size. This means that once some features of the solution are lost, the recovery based estimator is no longer able to capture them. As a consequence, as Δt grows, η^A tends to decrease and a mesh coarsening is induced. Since we resort to a recovery based approach also for time step adaptation, the solution-adaptation procedure enters into a coarsening loop, which may yield an endless increase of both the space and time discretization steps. In this concern our results confirm the conclusions drawn in [26] on a rather different problem setting. A practical remedy to avoid such a problem is to set carefully the tuning parameters involved into the space-time adaptation procedure, in particular the maximum time step and the minimum element number allowed during the computation. In the current test case, for instance, the value $\Delta t_{max} = 0.04$s turns out to be too big, so that

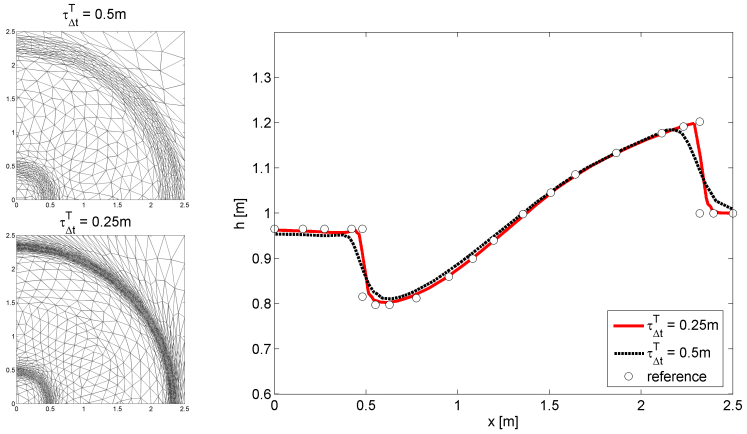

Figure 10: Radial dam break, $t = 1.5$s: adapted computational mesh for $\tau^T_{\Delta t} = 0.5$m (top-left) and $\tau^T_{\Delta t} = 0.25$m (bottom-left) and comparison of the adapted solutions with the reference solution (right).

when the tolerance $\tau^T_{\Delta t}$ is increased, Δt_{max} has to be reduced in order to avoid the progressive deterioration of the numerical solution.

5.2 Sudden wave propagation

We consider the propagation of a wave inside a closed basin. The basin is composed by a straight rectangular channel $[0, 30] \times [0, 10]$m and a squared basin of side 30m, joined by an asymmetric trapezoidal lateral expansion (see Figure 11). At $t = 0$s water is still inside the basin and the water depth is equal to 2m. A time-varying discharge Q is imposed on the left side of the basin. The inflow hydrograph is characterized by a linear increase of Q from 0 to 100m^3/s for $t \in (0, 10)$s, then the discharge remains fixed to 100m^3/s until the final simulation time, $T = 20$s. The effects of friction are neglected and the bottom of the basin is assumed flat. In Figure 11 we present some snapshots of a reference solution to describe the physical evolution of the phenomenon at hand. The reference solution is computed on a high-resolution grid of 53126 elements and by employing a fixed time step $\Delta t_R = 0.002$s. We can distinguish essentially three different phases during the evolution of the wave propagation process. During the first phase, as the wave propagates in the straight rectangular channel, the flow is essentially one dimensional (Figure 11, top left). Then for $t \in (6, 11.5)$s, the wave approaches the lateral expansion and the flow becomes really two dimensional (Figure 11, top right). In particular the solution is locally influenced by the presence of the sharp corner P. Finally, during the third phase, i.e., for $t \in (11.5, 20)s$, the wave undergoes multiple reflections inside the squared basin (Figure 11, bottom). This last phase turns out to be the most complex from a physical point of view, since the solution exhibits strong local features near the

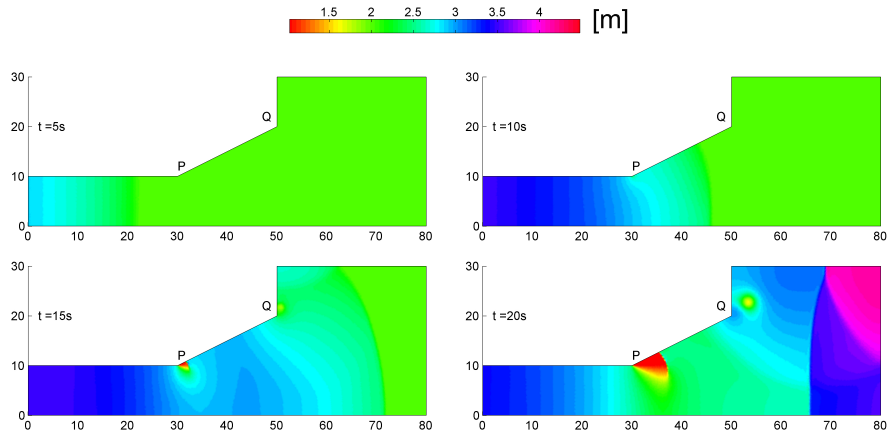

Figure 11: Sudden wave propagation: snapshots of the reference solution.

geometrical irregularities of the domain, i.e., the corners P and Q, and in correspondence with the three reflected waves. The same test case is run in [27] to assess the performances of the mesh adaptation procedure only, when combined with a fixed choice of the time step. We have chosen such a configuration as it is an archetypal of a real scale flow configuration and it exhibits different levels of complexity.

We consider now the results achieved by merging the adaptation of both the computational mesh and the time step. In particular we select the water depth h as the driving variable for the space-time adaptation. We set $\tau^S = 1$ and $\tau^T_{\Delta t} = 0.05$; moreover we impose the following limits to the parameters tuning the space-time adaptive procedure: $\Delta t_{min} = \Delta t^0 = \Delta t^1 = 0.02$s, $\Delta t_{max} = 0.3$s, $q_{min} = 0.02\text{m}^2$, $N_{el,min} = 400$.

Figure 12, left, shows the time evolution of the time step Δt and the corresponding progressive mean. The two trends allow us to follow the local value of the time step as well as to compare it with the mean of the previous values. The progressive mean provides the exact number k of adaptive time steps predicted to reach a certain simulation time. The trend of the time step is substantially characterized by three successive stages. In the first stage, for $t \in [0, 6.5)$s, the time step grows from the starting value $\Delta t^0 = 0.02$s, up to 0.3s. For $t \in [6.5, 11.5)$s, the time step progressively reduces to $\Delta t \approx 0.2$s. Finally, for $t \geq 11.5$s, the value of Δt is essentially set to the minimum allowed value, i.e., 0.02s. The final simulation time is reached after 462 time steps, so that the corresponding average time step is given by $\overline{\Delta t} = 0.043$s. The time evolution of the cardinality of the adapted mesh is shown in Figure 12, right. The trend exhibits two distinct phases: for $t < 11.5$s the number of elements preserves around 400, i.e., the minimum imposed via the metric correction $N_{el,min}$. Then, for $t \in [11.5, 20]$s, the number of elements grows, up to $N_{el} = 5500$.

We observe that the time evolution of both the adapted time step and the car-

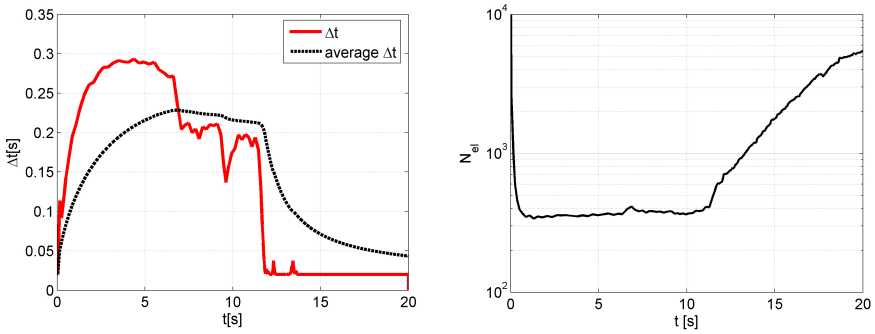

Figure 12: Sudden wave propagation: temporal evolution of the adapted time step (left) and of the number of elements of the adapted grids (right).

dinality of the adapted mesh is consistent with the evolution of the physical phenomenon. The three stages recognized in Figure 12, left, exactly reflect the three phases of the phenomenon itemized above. On the other hand the resolution of the adapted mesh is the minimum possible for the first two phases of the phenomenon, while it progressively increases during the third phase, i.e., in correspondence with the increasing complexity of the phenomenon at hand.
In Figures 13-15 we analyze the results associated with three different times which are representative for the three phases of the phenomenon; in particular we choose $t = 6.35$s, $t = 11.46$s and $t = 18$s. For each selected time, we show the spatial distribution of the water depth h and the corresponding adapted anisotropic grid used to compute it. Moreover, to assess the robustness of the solution-adaptation coupling, we compare the solution obtained via space-time adaptation with the reference solution in Figure 11. In more detail such a comparison is performed in correspondence with the longitudinal section highlighted in Figures 13-15, top left. The mean element area associated with the reference grid is 0.028m^2, i.e., of the same order of magnitude of the imposed q_{min}. On the other hand the fixed time step $\Delta t_R = 0.02$s corresponds to the minimum value Δt_{min} used in the adaptive simulation.
At $t = 6.35$s the wave propagation reaches the transition area between the straight and the divergent part of the channel (Figure 13, top left). At this time the predicted time step is $\Delta t_1 = 0.271$s while the mean time step computed on previous time intervals is $\overline{\Delta t} = 0.227$s (see Figure 12, left). Both these values are one order of magnitude larger than Δt_{min}. Concerning the adapted mesh (Figure 13, bottom-left), the elements in the straight channel are essentially stretched perpendicularly with respect to the one dimensional flow direction. Since the solution is constant along direction y, the limit of the element size along this direction coincides with the channel width itself. Moreover, the elements are mostly gathered in correspondence with the wave front. The solution computed via the space-time adaptive procedure shows a localized overdiffusion around the wave front position; anyway it coincides with the reference solution along most

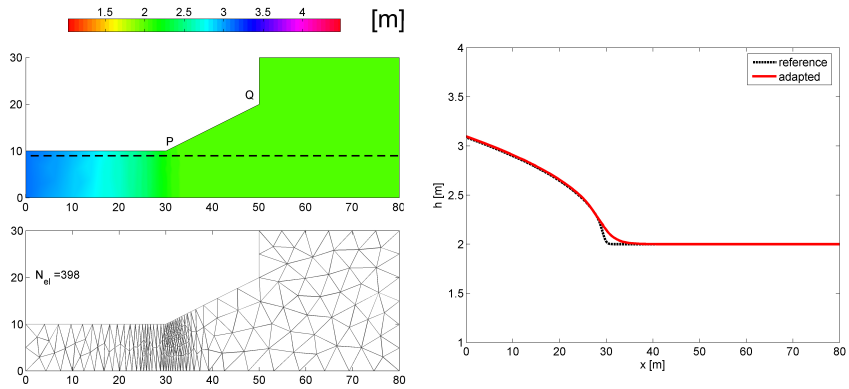

Figure 13: Sudden wave propagation, $t = 6.35$s: contour plot of the water depth h (top left), adapted computational mesh (bottom left) and comparison between the adapted solution and the reference solution (right).

of the considered section (Figure 13, right).

Similar conclusions can be drawn at time $t = 11.46$s, when the wave is approaching the squared basin (Figure 14). The time step is now $\Delta t = 0.178$s while the mean time step of the previous intervals is $\overline{\Delta t} = 0.212$s (see Figure 12). The elements cluster near corner P and around the front position, located about at $x \approx 55$m. Although the cardinality of the reference and adaptive meshes differ by two order of magnitude, the two solutions are very similar along the considered section (Figure 14, right). A localized overdiffusion characterizes the adaptive solution in correspondence with the wave front. On the basis of the considerations in section 5.1 a different tuning of the parameter involved would likely reduce the overdiffusion.

Let us focus now on $t = 18$s. The time step is $\Delta t = 0.02$s while the mean referred to the previous times is $\overline{\Delta t} = 0.05$s. The complex features of the phenomenon demand for a high resolution grid in many regions of the computational domain, in particular near the corners P and Q, and in correspondence with the reflected fronts. The reference and fully-adaptive solution are in really good agreement. However, the cardinality of the adapted mesh is one order of magnitude less than the one of the reference grid, while the $\overline{\Delta t} = 2.5\Delta t_R$. Despite the reduced number of elements, the wave fronts are sharply detected by the adapted solution (notice that the considered section crosses a reflected wave front about at $x \approx 72$m). We observe here a really slight phase difference between the reference solution and the fully adaptive one, which could be likely ascribed to the overdiffusion cumulated during the previous times.

To summarize, both the time step and the mesh adaptation procedure proved to be able to cope with the dynamics of the considered real-scale phenomenon. In particular the different phases characterizing the phenomenon find a full correspondence with the number of elements of the adapted mesh and with the

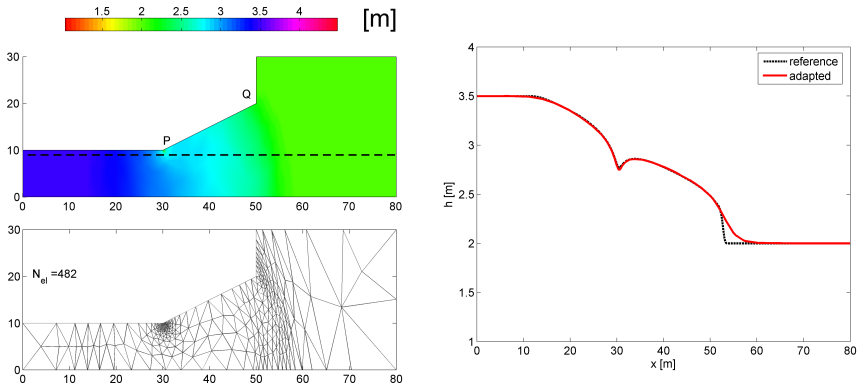

Figure 14: Sudden wave propagation, $t = 11.46$s: contour plot of the water depth h (top left), adapted computational mesh (bottom left) and comparison between the adapted solution and the reference solution (right)

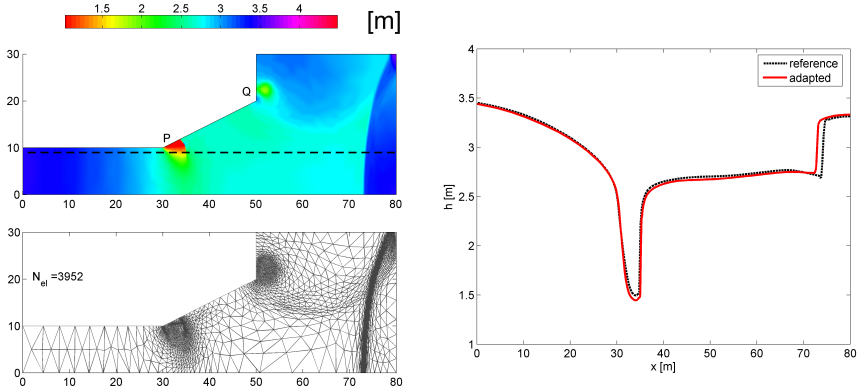

Figure 15: Sudden wave propagation, $t = 18$s: contour plot of the water depth h (top left), adapted computational mesh (bottom left) and comparison between the adapted solution and the reference solution (right).

chosen time step (a larger number of elements combined with a small time step are predicted for the most critical phases and vice versa). Some local inaccuracies given by a contained overdiffusion characterize the solution obtained via the space-time adaptation, in particular in correspondence with the wave fronts. However the global quality of the solution is preserved and the propagation of the local inaccuracies is limited in time.

6 Conclusions

We present in this work a space-time adaptation procedure for the approximation of the Shallow Water Equations. It is driven by a heuristic a posteriori estimator for the global error, which keeps separate the space from the time contribution. Both the space and time error estimators found on a recovered gradient approach. In particular we propose a new recovery procedure suited to the adopted time advancing scheme. On the other hand we rely on an anisotropic error estimator to drive mesh adaptation. A suitable adaptive procedure combining the information of the two error estimators with the chosen space-time discretization is finally set up.
We assess the coupled solution-adaptation scheme on two test cases. In particular we focus on the robustness of the proposed procedure. Results attest the general reliability of the whole procedure, even in the presence of rapidly varying flows and real scale phenomena.
The first test case helps us in understanding the crucial role played by the parameters of the adaptation procedure in terms of reliability. Indeed we highlight the possibility that an endless coarsening of both the space and time steps occurs, due to the interplay between the space and the time recovery based adaptations. To get rid of this matter, a suitable tuning of the control parameters which drive the space-time adaptation procedure turns out to be crucial.
Results of the real scale test case assess the capability of the proposed methodology to provide an accurate solution, by allocating the computational resources coherently with the evolution of the phenomenon at hand.
Future developments of the present work concern the application of the proposed adaptive procedure to different test settings, characterized, for instance, by larger evolutionary scales. In particular, we aim at investigating flooding phenomena influenced by complex geometries, typical, for example, of urban flooding simulations. Moreover, we are interested in the mathematical modeling of the propagation of wetting and drying fronts: this certainly represents an interesting issue where the potentiality of a space-time adaptation could provide considerable improvements both in terms of modeling accuracy and computational saving.

References

[1] M. Ainsworth , J.T. Oden, A Posteriori Error Estimation in Finite Element Analysis, Wiley, New York, 2000.

[2] R. Becker, R. Rannacher, An optimal control approach to a posteriori error estimation in finite element methods, Acta Numer. 10 (2001) 1–102.

[3] J.M. Cascón, L. Ferragut, M.I. Asensio, Space-time adaptive algorithm for the mixed parabolic problem, Numer. Math. 103 (2006) 367–392.

[4] Ph. Ciarlet, The Finite Element Method for Elliptics Problems, North-Holland, Amsterdam, 1978.

[5] Ph. Clément, Approximation by finite element functions using local regularization, RAIRO Anal. Numér. 9 (1975) 77–84.

[6] J.C. Dietrich, R.L. Kolar, K.M. Dresback, Mass residuals as a criterion for mesh refinement in continuous Galerkin shallow water models, J. Hydraul. Eng. 134(5) (2008) 520–532.

[7] P.E. Farrell, S. Micheletti, S. Perotto, An anisotropic Zienkiewicz-Zhu a posteriori error estimator for 3D applications, MOX Report 25/2009 http://mox.polimi.it/it/progetti/pubblicazioni/view.php?id=205&en=en.

[8] P.E. Farrell, S. Micheletti, S. Perotto, A recovery-based error estimator for anisotropic mesh adaptation in CFD, Bol. Soc. Esp. Mat. Apl. 50 (2010) 115–138.

[9] L. Formaggia, S. Perotto, New anisotropic a priori error estimates, Numer. Math. 89(4) (2001) 641–667.

[10] L. Formaggia, S. Perotto, Anisotropic error estimates for elliptic problems, Numer. Math. 94(1) (2003) 67–92.

[11] A. Hay, D. Pelletier D, R. Di Caro, Verified predictions of shape sensitivities in wall-bounded turbulent flows by an adaptive finite-element method, J. of Comput. Phys. 228(12) (2009) 4510-4531.

[12] F. Hecht, BAMG: bidimensional anisotropic mesh generator, http://www.ann.jussieu.fr/~hecht/ftp/bamg/.

[13] T.J.R. Hughes, M. Mallett, A new finite element formulation for computational fluid dynamics: III. The generalized streamline operator for multidimensional advective-diffusive systems, Comput. Methods Appl. Mech. Engrg. 58(3) (1986) 305–328.

[14] C. Johnson, A. Szepessy, On the convergence of shock-capturing streamline diffusion finite element methods for hyperbolic conservation laws, Math. Comp. 54(189) (1990) 107–129.

[15] T. Krámer, J. Jósza, Solution-adaptivity in modelling complex shallow flows, Comput. Fluids 36(3) (2007) 562–577.

[16] M. Krízek, P. Neittaanmäki, Superconvergence phenomenon in the finite element method arising from average gradients, Numer. Math. 45(1) (1984) 105–116.

[17] P. Lamby, S. Mueller, Y. Stiriba, Solution of shallow water equations using fully adaptive multiscale schemes, Internat. J. Numer. Methods Fluids 49(4) (2005) 417–437.

[18] R.J. Leveque, Finite Volumes Methods for Hyperbolic Problems, Cambridge University Press, New York, 2002.

[19] Q. Liang, A.G.L. Borthwick, Adaptive quadtree simulation of shallow flows with wetdry fronts over complex topography, Comput. Fluids 38(2) (2009) 127–162.

[20] J.L. Lions, E. Magenes, Non-Homogeneous Boundary Value Problems and Applications, Volume I, Springer-Verlag, Berlin, 1972.

[21] G. Maisano, S. Micheletti, S. Perotto, C.L. Bottasso, On some new recovery-based a posteriori error estimators, Comput. Methods Appl. Mech. Engrg. 195(37–40) (2006) 4794-4815.

[22] D. Meidner, B. Vexler, Adaptive space-time finite element methods for parabolic optimization problems, SIAM J. Control Optim. 46(1) (2007) 116–142.

[23] S. Micheletti, S. Perotto, Reliability and efficiency of an anisotropic Zienkiewicz-Zhu error estimator, Comput. Methods Appl. Mech. Engrg. 195(9–12) (2006) 799–835.

[24] S. Micheletti, S. Perotto, Anisotropic mesh adaption for time-dependent problems, Internat. J. Numer. Methods Fluids 58(9) (2008) 1009–1015.

[25] S. Micheletti, S. Perotto, Anisotropic adaptation via a Zienkiewicz-Zhu error estimator for 2D elliptic problems, Proceedings of ENUMATH 2009, the 8th European Conference on Numerical Mathematics and Advanced Applications, Springer-Verlag (in press).

[26] M. Morandi Cecchi, F. Marcuzzi, Adaptivity in space and time for shallow water equations, Internat. J. Numer. Methods Fluids 31(1) (1999) 285–297.

[27] G.M. Porta, S. Perotto, F. Ballio, Anisotropic mesh adaptation for shallow water modeling, MOX Report 1/2010 http://mox.polimi.it/it/progetti/pubblicazioni/view.php?id=216&en=en

[28] A. Quarteroni, Numerical Models for Differential Problems, Springer, Milano, 2009.

[29] J.-F. Remacle, S. Soares Frazão, X. Li, M.S. Shephard, An adaptive discretization of shallow water equations based on discontinuous Galerkin methods, Internat. J. Numer. Methods Fluids 52(8) (2006) 903–923.

[30] F.L.B. Ribeiro, A.C. Galeão, L. Landau, Edge-based finite element method for shallow water equations, Internat. J. Numer. Methods Fluids 36 (2001) 659–685.

[31] R. Rodríguez, Some remarks on Zienkiewicz-Zhu estimator, Numer. Methods Partial Differential Equations 10(5) (1994) 625–635.

[32] M. Schmich, B. Vexler, Adaptivity with dynamic meshes for space-time finite element discretizations of parabolic equations, SIAM J. Control Optim. 30(1) (2008) 369–393.

[33] F. Shakib, T.J.R. Hughes, Z. Johan, A new finite element formulation for computational fluid dynamics: X. The compressible Euler and Navier-Stokes equations, Comput. Methods Appl. Mech. Engrg. 89(1-3) (1991) 141–219.

[34] L.L. Thompson, D. He, Adaptive space-time finite element methods for the wave equation on unbounded domains, Comput. Methods Appl. Mech. Engrg. 194(18–20) (2005) 1947-2000.

[35] R. Verfürth, A review of A-Posteriori Error Estimation and Adaptive Mesh-Refinement Techniques, Wiley & Teubner, Chirchester, 1996.

[36] C.B. Vreugdenhil, Numerical Methods for Shallow-Water Flow, Kluwer Academic, Dordrecht, 1994.

[37] N. Yan, A. Zhou, Gradient recovery type a posteriori error estimation for finite element approximations on irregular meshes, Comput. Methods Appl. Mech. Engrg. 190(32–33) (2001) 4289–4299.

[38] O.C. Zienkiewicz, J.Z. Zhu Simple error estimator and adaptive procedure for practical engineering analysis, Internat. J. Numer. Methods Engrg. 23(2) (1987) 337–357.

[39] O.C. Zienkiewicz, J.Z. Zhu, The superconvergent patch recovery and a posteriori error estimates. I. The recovery technique, Internat. J. Numer. Methods Engrg. 33(7) (1992) 1331-1364.

[40] O.C. Zienkiewicz, J.Z. Zhu, The superconvergent patch recovery and a posteriori error estimates. II. Error estimates and adaptivity, Internat. J. Numer. Methods Engrg. 33(7) (1992) 1365–1382.

MOX Technical Reports, last issues

Dipartimento di Matematica "F. Brioschi",
Politecnico di Milano, Via Bonardi 9 - 20133 Milano (Italy)

13/2010 G.M. Porta, Simona Perotto, F. Ballio:
A Space-Time Adaptation Scheme for Unsteady Shallow Water Problems

12/2010 Riccardo Sacco, Paola Causin, Paolo Zunino, Manuela T. Raimondi:
A multiphysics/multiscale numerical simulation of scaffold-based cartilage regeneration under interstitial perfusion in a bioreactor

11/2010 Paolo Biscari, Sara Minisini, Dario Pierotti, Gianmaria Verzini, Paolo Zunino:
Controlled release with finite dissolution rate

10/2010 Alfio Quarteroni, Ricardo Ruiz Baier:
Analysis of a finite volume element method for the Stokes problem

09/2010 Laura M. Sangalli, Piercesare Secchi, Simone Vantini, Valeria Vitelli:
Joint Clustering and Alignment of Functional Data: an Application to Vascular Geometries

08/2010 Francesca Ieva, Anna Maria Paganoni:
Multilevel models for clinical registers concerning STEMI patients in a complex urban reality: a statistical analysis of MOMI^2 survey

07/2010 Laura M. Sangalli, Piercesare Secchi, Simone Vantini, Valeria Vitelli:
Functional clustering and alignment methods with applications

06/2010 Jordi Alastruey, Tiziano Passerini, Luca Formaggia, Joaquim Peiró:
The effect of visco-elasticity and other physical properties on aortic and cerebral pulse waveforms: an analytical and numerical study

05/2010 Matteo Longoni, A.C.I. Malossi, Alfio Quarteroni, Andrea Villa:
A complete model for non-Newtonian sedimentary basins in presence of faults and compaction phenomena

04/2010 Marco Discacciati, Paola Gervasio, Alfio Quarteroni:
Heterogeneous mathematical models in fluid dynamics and associated solution algorithms